

Article

Long-Term Deflection Analysis of Large-Span Continuous Prestressed Concrete Rigid-Frame Bridges Based on a Refined Modeling Approach

Xu Han , Wanheng Li and Pengfei Li *

Research Institute of Highway Ministry of Transport, Beijing 100088, China; cexuhan@163.com (X.H.); wh.li@rioh.cn (W.L.)

* Correspondence: pf.li@rioh.cn

Abstract: Numerical modeling approaches are favored for performing long-term analyses of continuous prestressed concrete rigid-frame (CPCR) bridges due to the complexity and high cost of experimental testing on such structures. In this study, a refined numerical modeling approach is first presented and validated by comparing the field monitor data of an existing long-span CPCR bridge in China. Then, long-term deflection analysis—considering box girder cracks, concrete creep, joint damage behavior and prestress—is conducted based on the proposed refined modeling approach. It is found that the time-dependent loss of longitudinal prestress has the most significant influence on the long-term structural stiffness, while joint damage between different segments has limited impact on overall structural performance, especially for large-span bridge cases. The local stress distribution is significantly influenced by typical damage, albeit with a different scope of impact. Therefore, targeted reinforcement has to be performed to achieve satisfactory repair results under different damage conditions.

Keywords: prestressed concrete rigid-frame bridges; refined modeling approach; performance degradation; long-term deflection; cause analysis



Citation: Han, X.; Li, W.; Li, P. Long-Term Deflection Analysis of Large-Span Continuous Prestressed Concrete Rigid-Frame Bridges Based on a Refined Modeling Approach. *Appl. Sci.* **2023**, *13*, 9727. <https://doi.org/10.3390/app13179727>

Academic Editors: Wenming Zhang, Xiaoming Wang, Yuan Sun and Hongyou Cao

Received: 21 July 2023

Revised: 23 August 2023

Accepted: 23 August 2023

Published: 28 August 2023



Copyright: © 2023 by the authors. Licensee MDPI, Basel, Switzerland. This article is an open access article distributed under the terms and conditions of the Creative Commons Attribution (CC BY) license (<https://creativecommons.org/licenses/by/4.0/>).

1. Introduction

Continuous prestressed concrete rigid-frame (CPCR) bridges combine the characteristics of T-shaped rigid frames and prestressed continuous beams, integrating piers and beams into a single structure with numerous engineering advantages. Firstly, since the piers of CPCR bridges are generally high, their flexibility can participate in the overall stress distribution, resulting in lower internal forces being generated in the main girder by temperature, prestress and shrinkage [1]. Additionally, this type of structure obviates the need for support required by conventional structures, thereby reducing construction time and lowering bridge operation and maintenance costs. As a result of these advantages, this type of bridge has been widely utilized in recent decades to span canyons and rivers, resulting in significant economic benefits, especially in China [2]. With increasing service time and the variability of service scenarios, the mechanical properties of numerous established CPCR bridges are deteriorating, resulting in mid-span deflection that will continue to increase through the years, without convergence. Table 1 lists some existing instances of CPCR engineering with excessive deflections. Excessive mid-span deflection in CPCR bridges has emerged as a primary constraint to its span development. Against this backdrop, numerous researchers have conducted experimental investigations on the evolution law of the mechanical properties of CPCR bridges under various deterioration patterns. Liu et al. presented an experiment and damage evaluation on a large-scale CPCR bridge with three spans and a total length of 18 m [3], and gave the change law of the mode shape curvature of the structure under the coupled conditions of steel bar yield and concrete cracking. Zong et al. conducted a collapse failure test on a scale model of a two-span

CPCR bridge under strong earthquake conditions [4]. The results of the test indicated that damage to the lower end of the central pier significantly reduced the seismic performance of continuous prestressed concrete rigid-frame bridges. Tong et al. conducted a field test investigating the cracking mechanism of CPCR bridges using the Wenchuan earthquake in 2008 as an example [5], on the basis of which it was concluded that the position most prone to cracking was the middle-span length between the 1/4 and 3/4 points of the total span. According to the above studies, it can be seen that existing experimental studies have been limited to only one or two influencing factors, due to constraints such as laboratory space and high experimental costs.

Table 1. Engineering examples of the excessive deformation of continuous rigid-frame bridges.

Bridge Name	Span Distribution (m)	Completion Year	Country	Mid-Span Deflection (cm)
Kingston Bridge	62.5 + 143.3 + 62.5	1970	United Kingdom	>30
Koro-Babeldaob Bridge	72 + 241 + 72	1978	Palau	120
Parrotts Bridge	99 + 195 + 99	1979	United States	63.5
Sanmenxia Yellow River Highway Bridge	105 + 4 × 160 + 105	1992	China	22
Stovset Bridge	220 (Main span)	1993	Norway	20
Jinsha Bridge	66 + 120 + 66	1994	China	22
Huangshi Yangtze River Bridge	62.5 + 3 × 245 + 62.5	1995	China	30.5
Jiangjin Yangtze River Bridge	140 + 240 + 140	1997	China	31.7
Auxiliary Channel of Humen Bridge	150 + 270 + 150	1997	China	22.2 (2003)
Stolma Bridge	94 + 301 + 72	1998	Norway	9.2 (2001)
Auxiliary Channel of Yajisha Bridge	86 + 160 + 86	2000	China	23

Excessive deflection of CPCR bridges is a complex systemic issue that arises from a multitude of factors influencing deterioration. Large deflections in bridges can result in girder cracking and prestress loss, all of which, in turn, further weaken the overall structural rigidity and accelerate bridge deformation [6]. Additionally, the long-term behavior of concrete, including creep and shrinkage, can also cause changes in the overall performance of CPCR bridges. Firstly, the long-term behavior of concrete induces internal force redistribution within the structure, resulting in prestress loss in the main beam [7]. Then, time-dependent properties may lead to the surface cracking of concrete [8]. Lastly, creep accelerates structural deformation and increases deflection, consequently causing an increase in initial eccentricity and generating secondary internal forces due to creep [9,10], especially during the winter period [11]. This weakens the bearing capacity of the control section. Numerical simulation methods have been widely accepted and recognized by scientific researchers since their inception due to the convenience of their application, the accuracy of their calculations and their clear theoretical foundations [12]. Given these advantages, refined numerical simulation approaches offer a reliable alternative for solving such engineering problems. As a result, they have been successfully applied on numerous occasions to predict bridge behaviors when considering different deterioration factors [13–16], thereby validating their wide applicability and high efficiency. Based on the above, numerical approaches are preferred over experimental methods for studying the long-term behavior of CPCR bridges and better understanding the effects of different damage parameters such as concrete cracking, creep, and prestress loss on the long-term deflection of CPCR bridges.

To investigate the primary cause of the long-term deformation of long-span CPCR bridges, this paper first presents a refined numerical modeling approach for the accurate modeling of CPCR bridges. Then, the validated refined model is utilized to determine the change law of the deflection curve of the main span under four performance degradation behaviors. Finally, an investigation is conducted into the local stress and deformation redistribution caused by box girder cracking, concrete creep, joint damage behavior and prestress loss.

2. Refined Numerical Modelling Approach

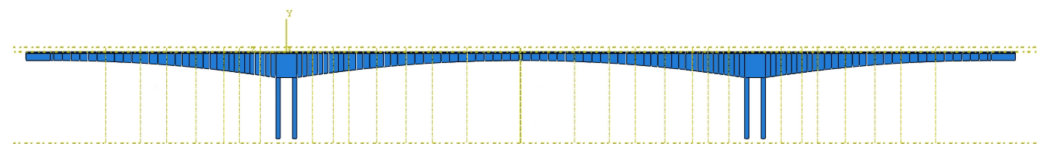
A numerical investigation was conducted on the long-term deflection of a continuous prestressed concrete rigid-frame (CPCR) bridge using the commercial finite element software ABAQUS. This section discusses key modeling modules and approaches for simulating various behaviors in ABAQUS, including prestress loss, temperature gradient, joint damage and concrete creep.

2.1. Base Model Parameters

A three-span CPCR bridge with spans of 150 m + 270 m + 150 m, constructed in Guangdong Province, China, in 1996, was selected as the base model for this study. The box-girder section was utilized and its height varied along the span direction. Specifically, the section height was 14.8 m at the end of the main span and decreased to 5.0 m at mid-span while maintaining a constant width of 15.0 m throughout the span length. For convenience, this bridge will be referred to as “Bridge A” hereafter. The main span of Bridge A was constructed using segmental assembly technology, with the entire bridge comprising a total of 131 segments and 63 segments forming the main span. These segments have been expertly assembled to create an integrated bridge structure. The site picture of Bridge A and its numerical segmental model are shown in Figure 1.



(a)



(b)

Figure 1. Schematic diagram of Bridge A: (a) size picture; (b) description of numerical segmental model.

2.2. Material Models

According to previous studies [17–21], the stress experienced by concrete materials during the service stage of a bridge is typically below 0.4 times its strength and is primarily in an elastic state. Therefore, numerical analysis often employs an elastic constitutive model to enhance the calculation efficiency. Given this fact, material nonlinearity was disregarded and the concrete was modeled using a linear elastic constitutive model. The elastic modulus and Poisson’s ratio of concrete are 3.45×10^4 MPa and 0.2, respectively. The rate of superstructure pouring concrete volume deviation was taken as 4% for a continuous concrete rigid-frame bridge, which was based on the statistical results achieved by Yu et al. [20], and the density could be determined as 2649 kg/m^3 . For prestress tendons, the modulus of elasticity, yield stress, Poisson’s ratio and density were $E = 1.95 \times 10^5$ MPa, $f_y = 1860$ MPa, $\mu = 0.3$ and $\rho = 7850 \text{ kg/m}^3$, separately, based on the design data, and

the ideal elastic–plastic model was chosen to simulate the stress–strain relationship of prestressed tendons. Based on the above description, the constitutive models of concrete and prestress are diagrammed in Figure 2. The cooling method was employed to induce prestress in the steel bar. For further information, refer to Section 2.5.4.

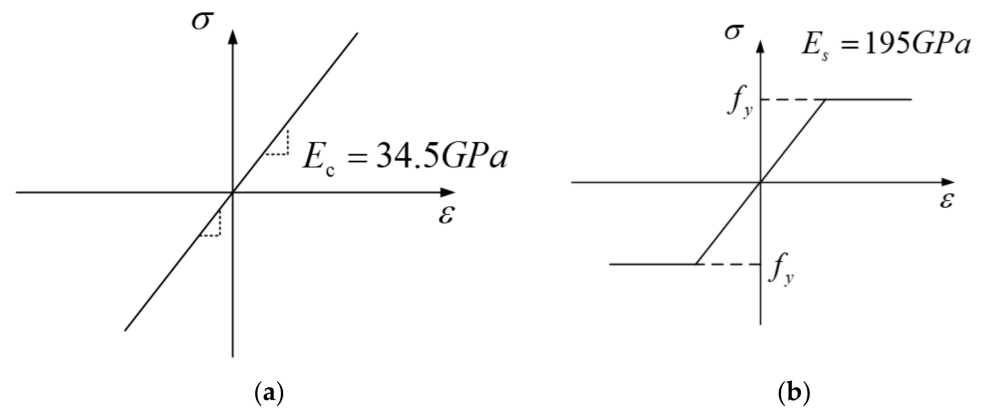


Figure 2. Constitutive model used for concrete and prestress tendons. (a) Linear elastic model for concrete. (b) Ideal elastic–plastic model for prestress tendons.

2.3. Element Selection and Mesh Division

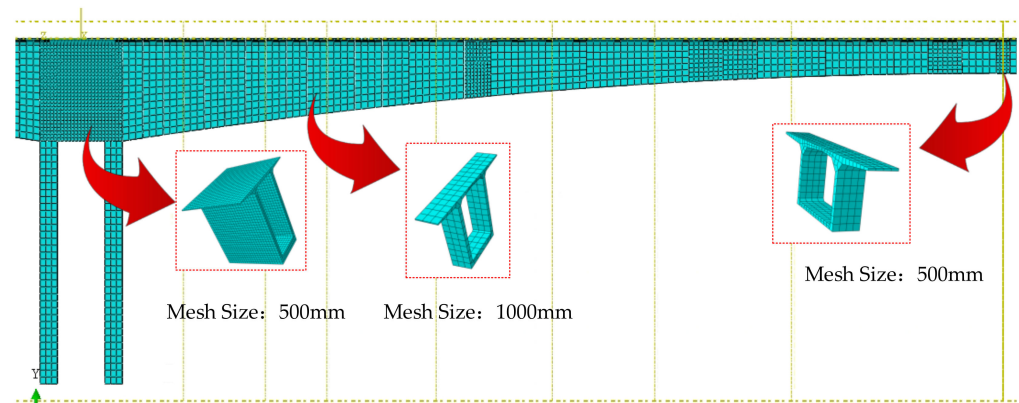
Generally speaking, beam elements and solid elements are usually used for the numerical simulation of concrete box girder bridges, and using beam elements for calculations often produces higher computational efficiency. However, the use of beam element models presents challenges in simulating certain behaviors: (1) Since the main beam is composed of beam elements, it becomes challenging to consider the crack condition even with certain section properties and geometric configurations. Typically, the attenuation method of cross-section concrete’s elastic modulus is employed to account for the impact of concrete cracking on section stiffness and mechanical properties. However, this approach fails to directly reflect crucial crack property parameters such as location, length, width, depth, and other relevant information. Additionally, it does not capture local stress changes resulting from stress concentration effects caused by cracks. (2) If the joint connection between beams is taken into consideration, the primary approach is to employ spring connections between nodes. However, due to the indeterminate value of spring stiffness, its mechanical characteristics cannot be accurately reflected in this model. Furthermore, the node–spring stiffness connection fails to precisely depict the joint state information. The beam element modeling method exhibits significant limitations in characterizing, extracting, and analyzing the mechanical properties of related joints and their impact on structural mechanics. Based on the above, the C3D8R solid element, available in ABAQUS, was selected to simulate the beams and piers of the CPR bridge.

The hexahedron shape was chosen as the basic element, and FE analysis utilized sweep technology combined with an advanced front algorithm [22]. The prestress tendons were simulated with the two-node linear 3D truss element T3D2. For optimal computational efficiency, a mesh sensitive study was conducted to determine grid number and layout, the results of which are listed in Table 2. Based on the optimal trade-off of calculation accuracy and time efficiency, the layout scheme of non-uniform 3D discretization along the span direction was determined, i.e., more mesh seeds were laid out in the unfavorable stress locations and a lower mesh density was set in the other area. The mesh division of the half main span of “Bridge A” is presented in Figure 3.

Table 2. Mesh convergence study results for element length along the bridge direction.

Nominal Element Length (mm)	Predicted Mid-Span Deflection (mm)	% Change in Deflection	Time Cost (Hours)
2000	87.73	−3.60	0.33
1000	89.90	−1.22	0.69
Non-uniform (Mix 500 and 1000)	90.78	−0.25	0.89
500	90.92	−0.10	1.67
250	91.01	-	4.41

System environment: Operation system: Windows 10. RAM: 16.0 GB. Processor: Intel® Core™ i7-6700K CPU @ 4.00 GHz 4.01 GHz.

**Figure 3.** Discretization of Bridge A in ABAQUS.

2.4. Interactions and Boundary Conditions

The translations and rotations at the bottom of the piers were fixed, while rotational degrees of freedom in all directions and translational degrees of freedom along the bridge were released at the end of span to simulate simply supported boundary conditions.

As the base model did not focus on joint damage behavior between different concrete segments, contact nonlinearity between them was neglected and a “Tie Constraint” was employed to simulate their interactions. The node-to-surface discretization method was adopted. The prestressed tendons were all embedded within the concrete beam regions.

2.5. Performance Degradation Simulation Approach

2.5.1. Box Girder Crack

The cracking of the box girder results in a local stiffness loss, which causes an increase in deflection and stress redistribution near the crack area. Among the existing simulation techniques, there are two main methods to simulate the post-crack behavior of concrete, called the smeared crack model and the discrete crack model, respectively.

The former method simulates cracks equivalently through inelastic cracking strains. Essentially, crack development is predicted by adjusting the material softening constitutive relationship with the fracture energy conservation criterion. Since the smeared crack model needs to consider the softening behavior of the concrete, the iterative step is usually required to be very small, leading to a slower solution speed. The discrete crack model describes the discontinuous displacement field formed by the crack by setting interface elements at the crack position. The advantage of this model is that the crack area can be preset and the stiffness reduction and stress concentration effects caused by cracking can be considered, and these are widely used to analyze the mechanics issues with cracking paths. Existing studies have shown little difference between the above two models in the prediction of mechanical results [23]. For the case of predicting the long-term performance and post-crack behavior of the CPCRC bridge, the crack position is already determined, and the discrete crack model is usually appropriate to use. The sketches of the above two methods are presented in Figure 4.

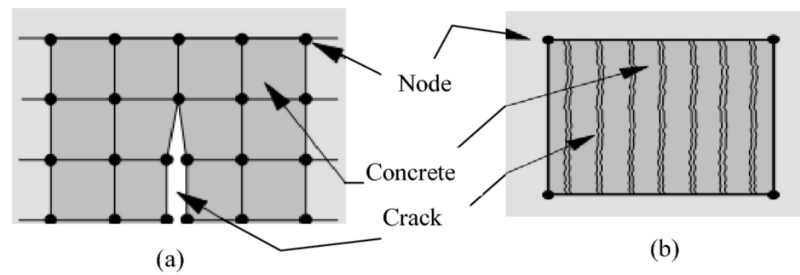


Figure 4. Concrete cracking models: (a) discrete crack model; (b) smeared crack model (reproduced from [24]).

The 270 m main span consists of 65 segments in total. Except for the mid-span closure segment, two identical segments are arranged symmetrically along the left and right half, respectively. For ease of distinction, the segment located in the right half of the bridge is labeled X, and that in the left half of the bridge is labeled X'. The numbering rules for each segment in the main span of Bridge A are shown in Figure 5.

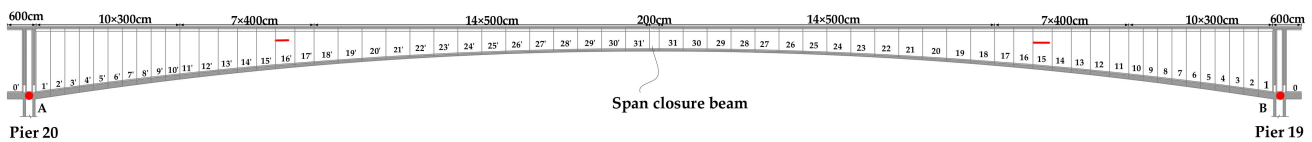


Figure 5. Segmental numbering rules for the main span of Bridge A.

In order to accurately simulate the structural behavior, on-site crack monitoring was carried out. According to the field investigation, more than 1000 cracks were found based on the ultrasonic testing method, and most of them were shallow cracks. Considering the computational efficiency of the model, it was not feasible to incorporate all the cracks into the model. Given that the box girder structure is a bending-shear coupling force system, two obvious cracks near the bend-shear coupling region were selected for analysis. These cracks are indicated by red lines in Figure 5 and were chosen to maximize their impact on the bridge beam structure. To investigate the characteristics of cracks, four concrete core samples were drilled outside both webs near the location of the crack. The core drilling process and the core sample are presented in Figure 6, and it can be seen that the crack had penetrated the concrete core samples. The crack dimensions obtained using the drilling method are listed in Table 3, and the preset crack zone of the box beam can be built initially in the Part module in ABAQUS, as can be seen in Figure 7.

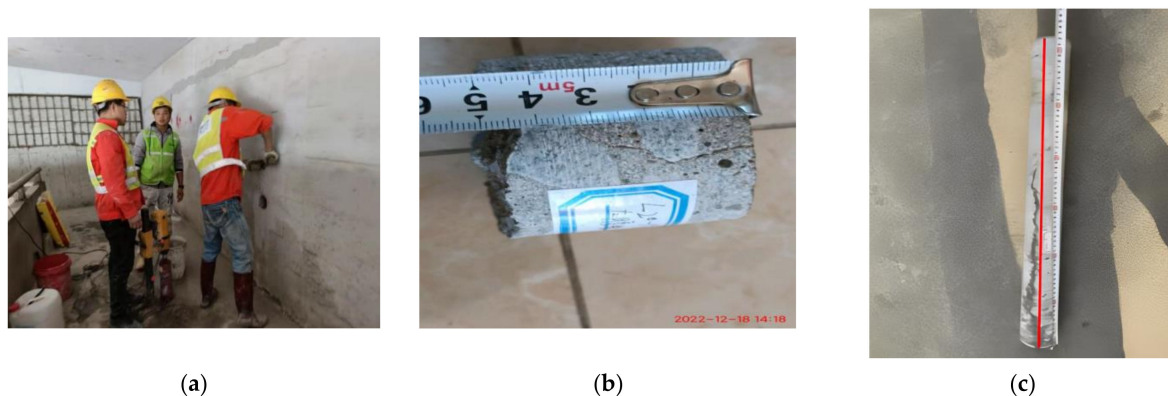


Figure 6. Drilling process and the core samples: (a) drilling process; (b) core splitting; (c) penetrated cracks.

Table 3. Crack information near the quarter span of Bridge A.

Locations	Length of the Crack (mm)	Width of the Crack (mm)	Diameter of Drilling Core (mm)	Depth of Drilling Core (mm)
Web of No.15 box beams	3170	0.26	50	130, 160
Web of No.16' box beams	2800	0.20	70	180

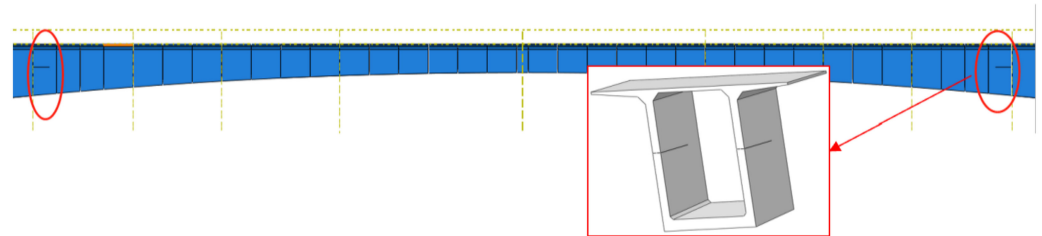


Figure 7. Schematic diagram of the three-dimensional finite element model for box beam cracks.

2.5.2. Concrete Creep

As a time-varying material, the creep development of concrete will cause its mechanical properties to change with service time. It is generally believed that the creep strain develops most rapidly at the initial stage of bridge construction, and then as the service time of the bridge increases, the concrete hydration gradually becomes sufficient and the creep development tends to become stable. The age-adjusted effective modulus (AAEM) method proposed by Trost [25] and modified by Bazant [26] was used within this study to consider the long-term performance of Bridge A as affected by creep. The effective modulus E_{eff} can be obtained from:

$$E_{eff} = \frac{E(t_0)}{1 + \chi(t, t_0)\varphi(t, t_0)} \tag{1}$$

$$\chi(t, t_0) = \frac{1}{1 - e^{-\varphi(t, t_0)}} - \frac{1}{\varphi(t, t_0)} \tag{2}$$

where $E(t_0)$ denotes the tangential elastic modulus of concrete at initial loading time t_0 ; $\varphi(t, t_0)$ is the dimensionless creep coefficient, which indicates the ratio of creep strain to the elastic strain of concrete from the initial time t_0 to the current time t ; and $\chi(t, t_0)$ is the aging coefficient of concrete, and its relationship with the creep coefficient is shown in Formula (2).

The calculation method of creep coefficient $\varphi(t, t_0)$ given in the current Chinese Industry Specifications [27] was adopted to take into account the creep effect. The related expressions are listed within Equations (3)–(5):

$$\varphi(t, t_0) = \varphi_n(t, t_0) \left[\frac{(t - t_0)/t_1}{\beta + (t - t_0)/t_1} \right]^{0.3} \tag{3}$$

$$\beta = \min \left\{ 150 \left[1 + (1.2RH)^{18} \right] \frac{h}{h_0} + 250, 1500 \right\} \tag{4}$$

$$\varphi_n(t, t_0) = \frac{5.93 \left(1 + \frac{1 - RH}{0.46(h/h_0)^{\frac{1}{3}}} \right)}{\left(\frac{f_{cu,k}}{f_{cmo}} + 1 \right)^{0.5} \left[0.1 + \left(\frac{t_0}{t_1} \right)^{0.2} \right]} \tag{5}$$

where $\varphi_n(t, t_0)$ is the nominal creep coefficient and can be obtained with Equation (5); h represents the equivalent thickness (mm), which can be expressed as $2A_c/C_c$, where A_c is the area of the concrete section (mm²) and C_c is the circumference of the concrete section in contact with the atmosphere (mm); $f_{cu,k}$ is the standard value of compressive strength of

the concrete cube (MPa); $h_0 = 100$ mm, $t_1 = 1$ d and $f_{cm0} = 10$ MPa are reference thickness, reference time and reference strength, correspondingly; and RH is the abbreviation of the relative humidity of the environment.

Within this study, the starting time t_0 was taken as 7 days. Due to differences in the construction completion time of different segments, the creep times of each segment were also different. However, since the creep development process is slow and gradual, especially the period from the completion of the whole bridge construction (around 400 days) to the late operation stage (10,000 days), the difference in the creep process caused by the difference in construction age is quite limited. Therefore, for the whole-bridge model analysis, the above age differences were negligible.

It can be concluded that different creep strains occur within different segmental box beams with unequal equivalent thicknesses. In this study, the No.0 box beam above the pier was adopted due to its minimum equivalent thickness, which caused conservative analysis results. Based on the above algorithm, the modulus of concrete was taken as 83.4% of the designed modulus to consider the stiffness degradation caused by creep, which can be directly input into the material properties of the FE software.

2.5.3. Joint Damage Behavior

To study the joint damage behavior between segments, the shear-friction theory discussed in detail by Philip and Halvard [28] was adopted within this study to equivalently simulate the discontinuous mechanical behavior between joints. The shear-friction theory assumes that a crack has occurred along the shear plane, and when a slip occurs along the crack the pieces of concrete on either side of the crack will be made to separate slightly due to the existence of a rough crack face. This separation will create an extra compressive stress zone near the concrete zone, which would provide more resistance to slip behavior by virtue of friction. Within this case, the below equation holds:

$$v_u = \sigma_x \tan \phi = p f_y \tan \phi \quad (6)$$

where v_u indicates the shear strength; p is the reinforcement parameter; f_y means the yield stress of reinforcement; and $\tan \phi$ denotes the coefficient of friction.

Shear-friction theory can be achieved in ABAQUS with penalty friction formulation, which can be defined in the tangential behavior of contact property module. The value of the friction coefficient takes 1.40 for a rough, bonded interface between cast-in-place concrete where intermediate grade reinforcement is used [29]. The limit shear stress of concrete was set as 4.2 MPa. "Hard" behavior was adopted to simulate the normal behavior between adjacent segments.

2.5.4. Prestressing

The spatial prestress was applied in ABAQUS, and the arrangement of prestress tendons in different directions can be seen in Figure 8. From the prestress reinforcement layout, the cracks that occur in Figure 7 may be attributable to the inadequate positive bending moment bearing capacity resulting from the limited prestressed length of the bottom plate, as observed from the perspective of the prestressed reinforcement layout. Internal prestress can be applied via the cooling method, and can be achieved by setting specified predefined fields. The relationship between the prestress value σ_p and the applied temperature field is as follows:

$$\sigma_p = \alpha E \Delta T \quad (7)$$

where ΔT is the temperature difference with the unit $^{\circ}\text{C}$; E represents the elastic modulus of prestress tendons (MPa); and α is the linear expansion coefficient.

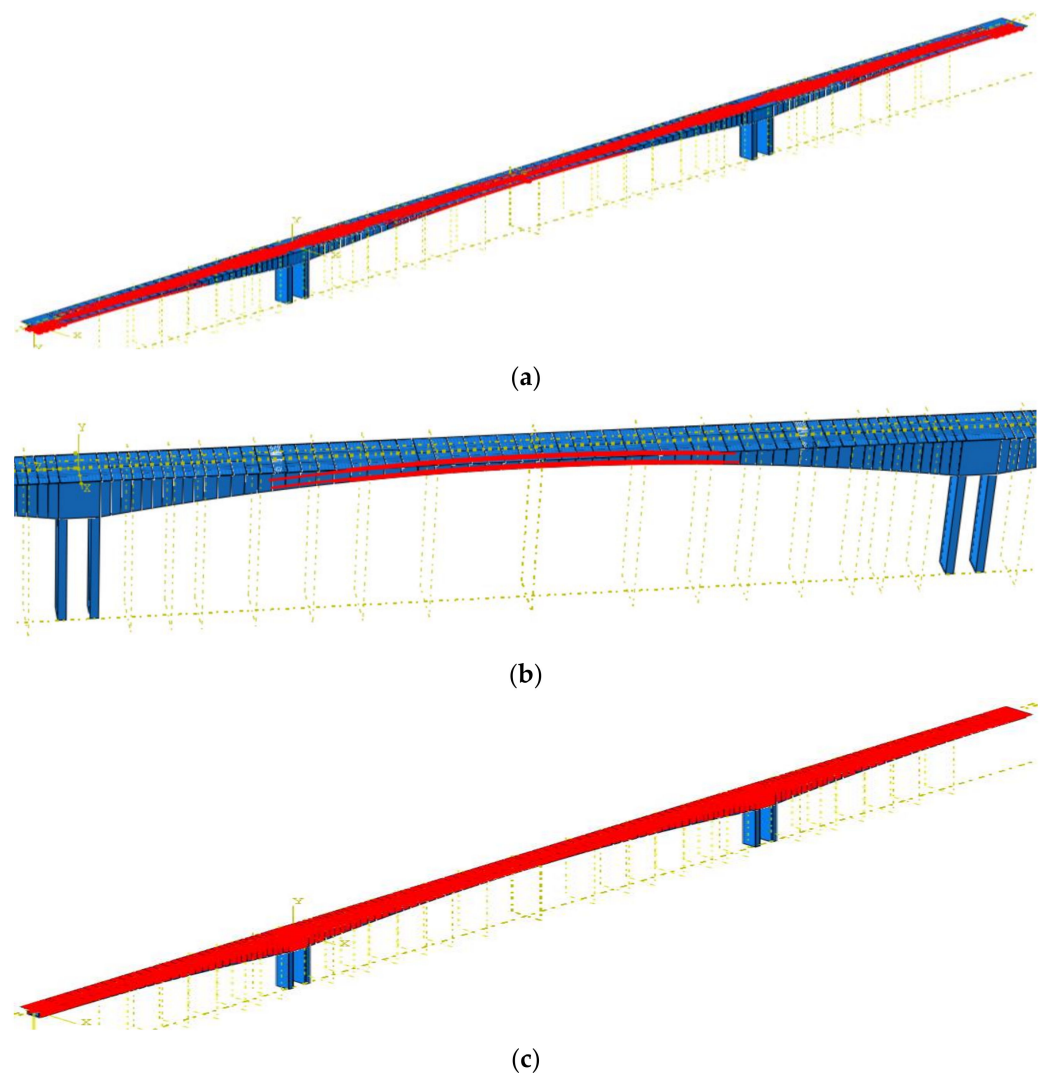


Figure 8. Embedded spatial prestress tendons in FE software: (a) longitude prestress; (b) partial amplification of main-span prestressed tendons on the bottom plate of a box beam; (c) horizontal and vertical prestress.

In order to grasp the spatial prestress state, the horizontal, vertical, and longitudinal prestress tendons at different positions of Bridge A were field tested, and three field test methods were used, the transverse tension method, stress release method and the X-ray diffraction method, as can be seen in Figure 9. The first two methods have been widely employed in the field of bridge detection due to their well-established theoretical foundation and convenient operational procedures [30–33]. The X-ray diffraction method was first proposed in 1987 [34] and is widely recognized as one of the most powerful nondestructive tools for measuring residual stresses in polycrystalline materials, and it has been extensively employed both in service and laboratory research, where it yields satisfactory predicted results [35,36]. In this paper, the X-ray diffraction method was first used in the prestress testing field, and the X-ray testing machine was self-developed as well. During the test, the instrument was required to align the center of the test point, the center of the X-ray spot, and the center of rotation of the goniometer. The instrument examined changes in lattice spacing within prestressed tendons by utilizing the X-ray diffraction approach and converted them into actual stress values using Bragg's equation.



Figure 9. Three kinds of prestress test method: (a) transverse tension method; (b) stress release method; and (c) X-ray diffraction method.

The on-site test results are listed in Table 4. The loss rate mentioned in Table 4 refers to the effective prestress value tested in the field divided by the design stress value of the prestress (1395 MPa). For all the analyses presented below, unless specified otherwise, the average loss rate in three directions has been adopted within the analysis.

Table 4. Field test results of prestress state.

Prestress Direction	Test Locations	Test Method	AVG/SD ¹ of Loss Rate (%)	95% Confidence Interval of Prestress Loss Rate (%)
Horizontal	1/4 span position	Transverse tension method	45.4/18.1	[36.8, 53.9]
Vertical	1/4 span position	Stress release method	68.6/16.1	[62.7, 74.6]
Longitudinal	Whole-bridge range	X-ray diffraction method	29.0/17.5	[20.4, 37.6]

¹ AVG = Average value and SD = Standard deviation.

2.5.5. Reinforcement Behavior

Bridge A was reinforced with CFRP cloth and external prestress tendons in July 2006. Hence, reinforcement behaviors including external prestress and CFRP cloth are simulated within this model.

The external prestressed tendons were modeled by virtual prestressed elements. Virtual prestressed element modeling primarily involves the connection between the virtual steel bundle and the actual steel bar through a spring mechanism. Specifically, a small section of the virtual steel bar is embedded within the concrete box girder bottom plate to establish contact with both the external prestressed steel bar and the real steel bar via spring connections. The stiffness of these springs is set to infinity, the purpose of which is to realize the linkage contact relationship between external prestressed steel bars and real steel bars.

The thickness direction of the CFRP sheet was much smaller than the other two directions, and the stress change along its thickness direction was relatively small, so the shell element was selected for modeling. The CFRP sheet was affixed to the web of the box girder in order to impede crack development in the web section, which could be considered as an elastic material. Considering that reinforcement behavior of the CFRP sheet does not occur during initial operation, it remains necessary to record subsequent reinforcement locations' cooperative deformation for activating the shell-unit-simulating CFRP sheet at a later stage. To achieve this objective, this paper employed the virtual steel plate method for simulation. Specifically, a virtual steel shell element with a stiffness of 0 was arranged on the web of the box girder, enabling it to co-deform with the box girder. Once a predetermined deformation level had been reached, the activation of the CFRP sheet occurred at the position where the virtual steel plate was located and their contact relationship was set as "Tie" to accomplish structural constraint via the CFRP sheets. The above two methods are shown in Figure 10.

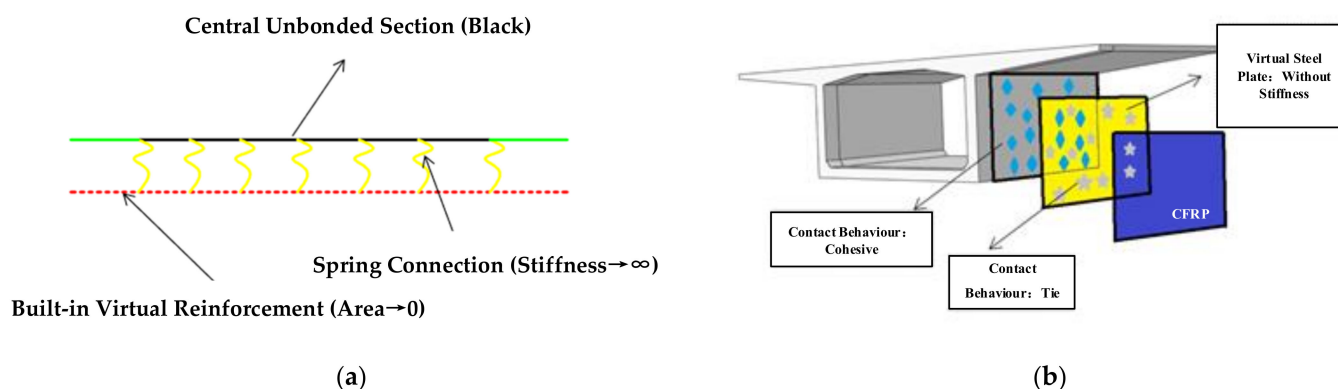


Figure 10. Modelling approach of reinforcement behavior: (a) external prestress tendons modelling approach; (b) virtual steel plate method.

2.6. Loading Scheme

Bridge deck pavement loads and lane loads were sequentially added to the model. Similar to the study of Yu et al. [20], the volume deviation rate of the bridge deck pavement was also investigated and an average deviation rate of +68.5% was obtained according to the statistical results of field measurements. The pavement loads, considering the volume deviation, were applied by the form “Pressure” with a magnitude of 3.37 kN/m^2 . Each lane load was composed of a uniform load of 10.50 kN/m and a mid-span concentrated load of 360 kN , which is specified in the Chinese design code [27], and a total of four traffic lanes were set. The load arrangement was selected according to the most unfavorable condition that caused the maximum deflection at the mid-span position.

3. Numerical Validation and Results

3.1. Validation of the Numerical Model

In order to verify the accuracy of the proposed numerical model, its results were extracted and compared with long-term monitoring data. The comparison results are presented in Figure 11. It should be noted that the determination of concrete’s elastic modulus at different service times followed the theory described in Section 2.5.2. Additionally, due to a lack of field test data at various service times, it was assumed that prestress loss rates increased linearly over time, and the final prestress loss rates of all tendons are listed in Table 4. It can be observed that the gap in the mid-span deflection between the measured and predicted data was narrow, with a maximum error of -2.8% . It can be concluded that the gap between the model predictions and the measurements became wider after reinforcement; even so, the maximum error was still less than -5% . It can be seen that the proposed FE model in the current paper provided a good agreement with the field test results, validating that the accuracy of the refined simulation method could be used to predict the structural performance of CRPR bridges.

In the following sections, a meticulous investigation is carried out on the impact of concrete cracks, concrete creep age, joint damage and prestress loss on the overall stiffness of Bridge A. In order to ensure the generalizability of the findings for general CPR bridge cases, the models without reinforcement measures were the most appropriate to select as the base models for analysis. To ensure comparability, other parameters were taken as design data when conducting sensitivity analysis on specific variables.

3.2. Crack Pattern

Three crack patterns were selected and are compared in this section: single-sided non-penetrating cracks (Pattern A#), single-sided penetrating cracks (Pattern B#) and both-sided penetrating cracks (Pattern C#), respectively [37]. These chosen patterns are illustrated in Figure 12, with the applied crack position remaining consistent with that shown in Figure 5.

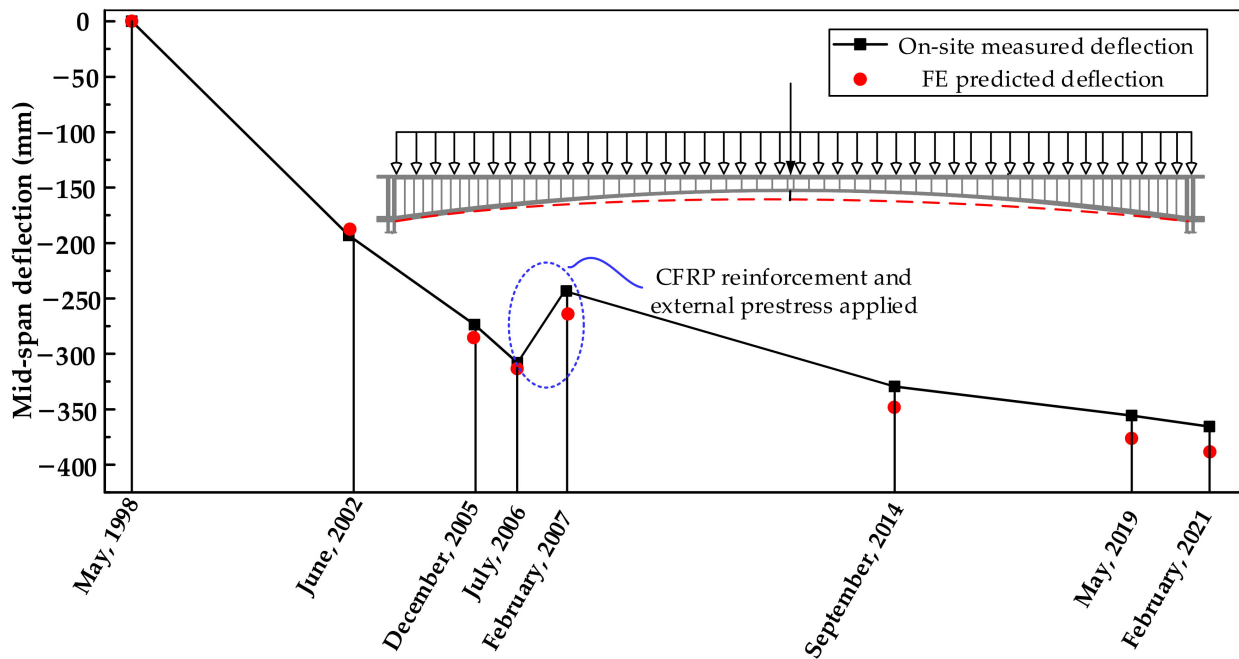


Figure 11. Mid-span deflection comparison between the on-site-measured and FE-predicted deflection.

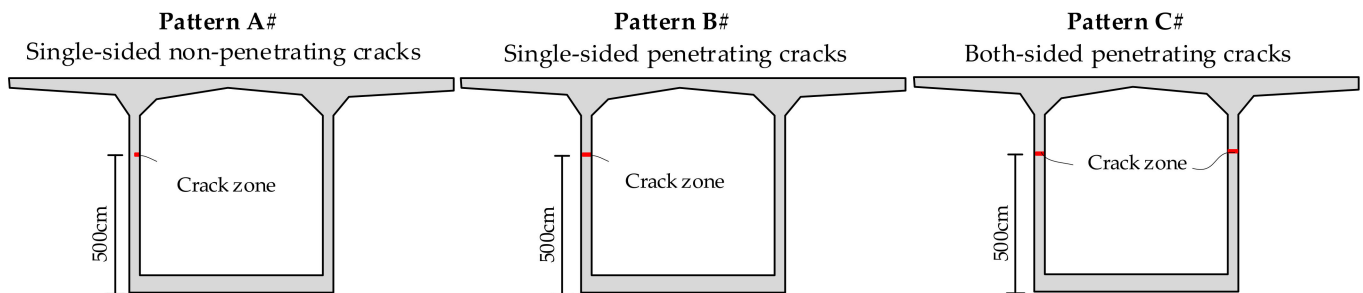


Figure 12. Three applied crack patterns in the FE software.

Figure 13 illustrates the deflection curves corresponding to different crack patterns, with the abscissa denoting the distance from point A in Figure 4 to the testing location. It can be observed that distinct modes of cracking correspond to specific characteristics in the deflection curve. A lower distribution of cracks results in shallower cracks and a smoother deflection curve. Furthermore, a comparison can be made between the maximum deflection values with and without cracks. A significant discrepancy can be observed, indicating that cracking has a substantial impact on the overall stiffness of the structure. Specifically, an average degradation of 33% in stiffness was identified in this case. For all three crack patterns, the maximum deflection was observed in the case of a both-sided penetrating crack with a value of 142.7 mm. In pattern A#, the maximum deflection was 132.7 mm, and in pattern B# it was 137.5 mm. Similarly, by comparing the deflection amplitude at the cracking positions ($x = 54$ m, 216 m), it can be inferred that the difference in deflection is relatively insignificant. Therefore, it can be concluded that the cracking mode of the box girder not only affects its maximum response but also influences the distribution of deflection along the bridge.

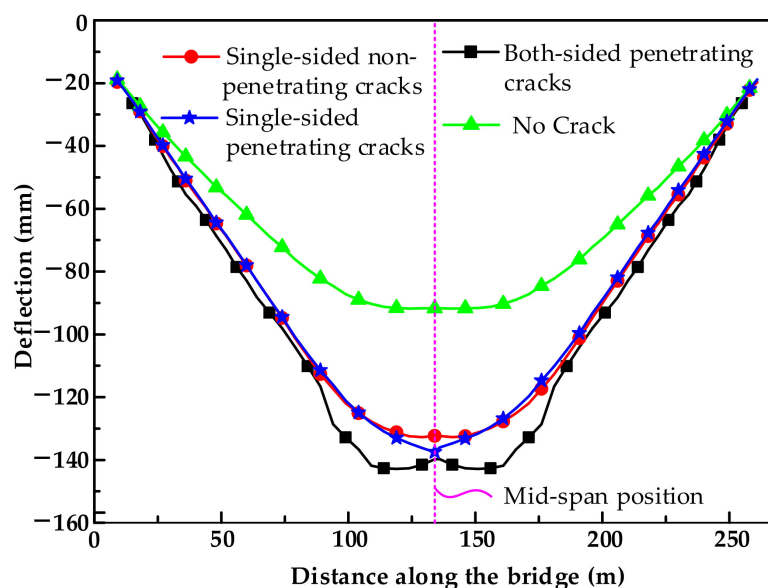


Figure 13. Deflection for different crack patterns.

3.3. Creep Age of Concrete

To investigate the time-dependent behavior of the CPCRB Bridge, the bridge at the operation time (400 days), at 1095 days (3 years), 3650 days (10 years), and at 10,000 days (current age) were selected for an analytical model, and the adjusted modulus at different service times can be determined using Equation (1). Within this model, no cracking was applied to the beam.

The deflection clusters, which take into account the long-term effects, are summarized in Figure 14. It is evident that the maximum deflection of the main span increased with service time; its downward deflection rate gradually decreased, however, which is consistent with the creep development rule of concrete. Using the bridge upon completion of construction as a baseline, Bridge A exhibited mid-span deflection increases of 16.9%, 28.8%, and 33.0% at 3, 10, and 30 years, respectively. Moreover, the creep of the concrete gradually reached a state of stabilization after 10 years of development, as indicated by the analysis results presented in Figure 14.

3.4. Joint Damage

The present section investigates the impact of joint damage degree and quantity on overall bridge performance. To conduct a sensitivity analysis, six cases were selected, including three types of joint damage degrees (DJ-1, DJ-2, DJ-3) and three ranges of damaged joints (RJ-1, RJ-2, RJ-3). The corresponding joint damage statuses are described in Table 5.

Table 5. Summary of the joint damage case.

Analysis Case	Description
DJ-1	Mid-span joint set to “contact” behavior with friction coefficient 1.40
DJ-2	Mid-span joint set to “contact” behavior with friction coefficient 1.00
DJ-3/RJ-1	Mid-span joint set to “contact” behavior with friction coefficient 0.70
RJ-2	All joints from the position of 3/8 span to 5/8 span set to “contact” behavior with friction coefficient 0.70
RJ-3	All joints from the position of 1/4 span to 3/4 span set to “contact” behavior with friction coefficient 0.70
No damage condition	“Tie Constraint” is employed to simulate each interaction.

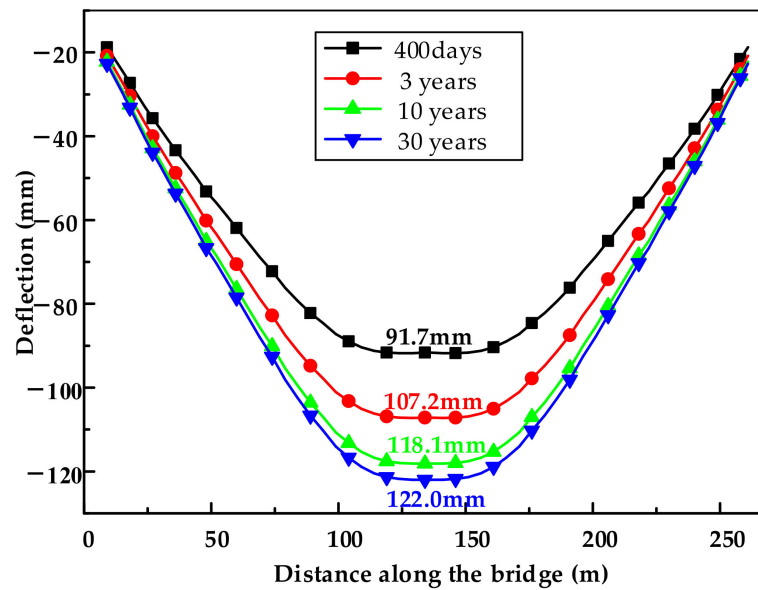


Figure 14. Deflection for different creep ages.

The comparison results of deflection curves under different joint damage conditions are presented in Figure 15. It can be observed that, regardless of the extent of joint damage for discretized joint damage types (DJ Series), it had a negligible impact on the overall stiffness distribution of the structure. For the segment with continuous damage joint distribution, the wider the range of joint damage, the wider the range of beam stiffness redistribution, and the greater the corresponding mid-span deflection. Specifically, for RJ-2 and RJ-3 conditions, there was an increase in the maximum mid-span deflection by 2.7% and 5.4%, respectively, compared to undamaged conditions. In fact, for small-span CPCBR bridges, the impact of joint damage was generally significant, particularly at the quarter position. This was due to the larger shear ratio of quarter spans under small span conditions, which necessitates higher joint requirements. For long-span CPCBR bridges, however, section bending moment dominated and limited the effects of joint damage on structural integrity.

3.5. Prestress Loss

The investigation focuses on the impact of prestress loss in various tendons on bridge performance, with prestress loss rates determined at 33.3%, 66.7% and 100% of the average values listed in Table 4. The adopted case is presented in detail in Table 6.

Table 6. Summary of the prestress loss case.

Analysis Case		Horizontal Prestress Loss Rate (%)	Vertical Prestress Loss Rate (%)	Longitudinal Prestress Loss Rate (%)
Horizontal and vertical prestress loss combinations	Case I	15.1	22.9	-
	Case II	30.3	45.7	-
	Case III	45.4	68.6	-
Longitudinal prestress loss conditions	Case IV	-	-	9.7
	Case V	-	-	19.3
	Case VI	-	-	29.0
No loss condition	Case VII	-	-	-

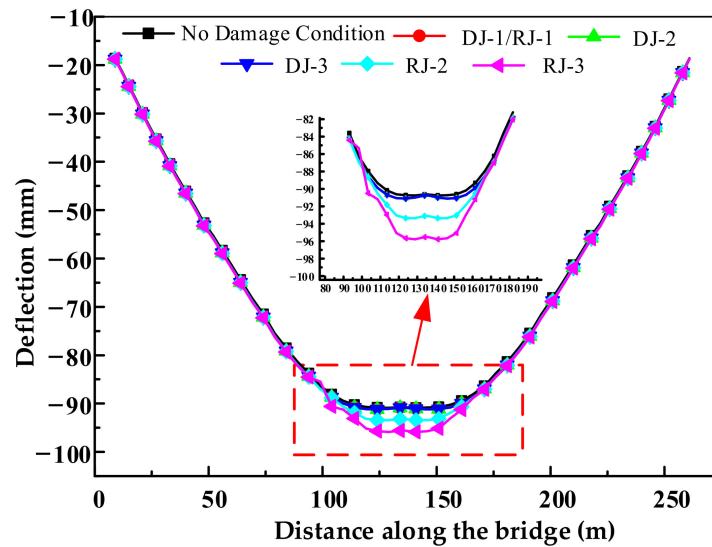


Figure 15. Deflection for different joint damage conditions.

Figure 16 illustrates the deflection relationship under various prestress loss conditions. It is evident that the combined horizontal and vertical prestress loss had a negligible impact on the overall deformation performance of the bridge, except for its effect on local force and the deformation of the box girder, which will be discussed in detail later. However, longitudinal prestress loss exerted a significant influence on overall stiffness. Compared with the no-prestress-loss condition, the maximum deflection of the main-span bridge increased by 87.2%, 172.8%, and 260.0% for Case IV, Case V, and Case VI, respectively.

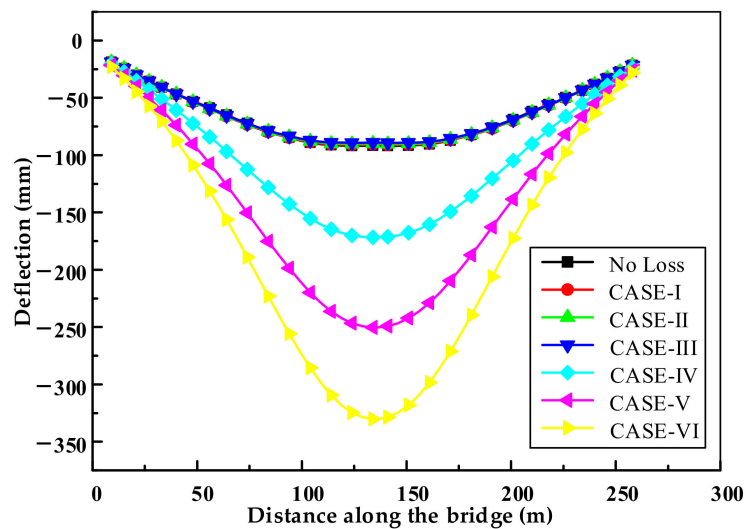


Figure 16. Deflection for different prestress loss conditions.

After a comprehensive comparison of the aforementioned four types of damage behaviors, it can be concluded that the primary cause for long-lasting deflection in continuous rigid frame bridges is attributable to the time-dependent loss of longitudinal prestress. In detail, sensitivities to the impact on the overall performance of the structure ranged from significant to slight: longitudinal prestress loss, box girder crack, concrete creep, continuous joint damage, and horizontal and vertical prestress loss to discrete joint damage, respectively.

4. Discussion

In the preceding chapter, the impact of typical defects in CPRC bridges on their overall structural stiffness was elaborated on. In this section, our primary focus is on examining changes in local mechanical properties of bridges under various damage conditions. The symbols used in the operating condition description are consistent with those introduced in the preceding chapter. In Figures 17–20, the legend generated by the ABAQUS calculation results uses the float constant format instead of scientific notation. The relationship between them is as follows: $Ae \pm n = A \times 10^{\pm n}$, for example, $2.17e-03 = 2.17 \times 10^{-3} = 0.0217$.

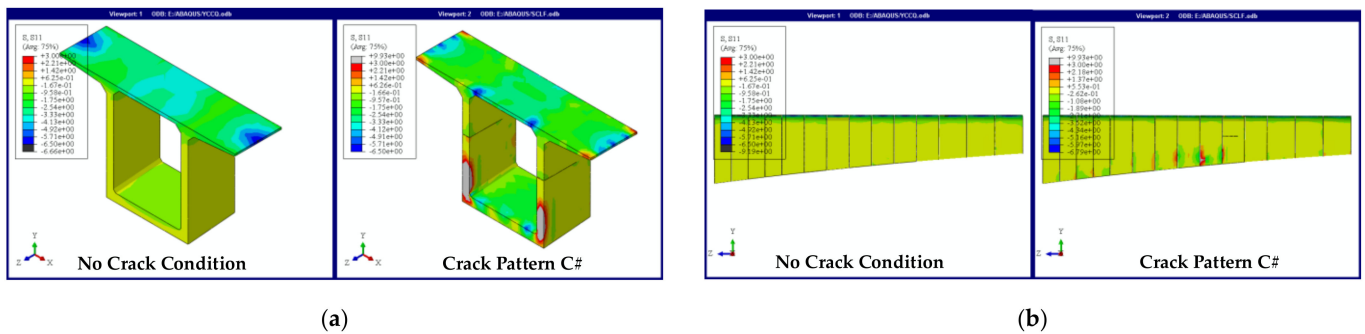


Figure 17. Stress distribution comparison between crack Pattern C# and no crack condition. (a) Stress distribution of single segment. (b) Quarter-span range.

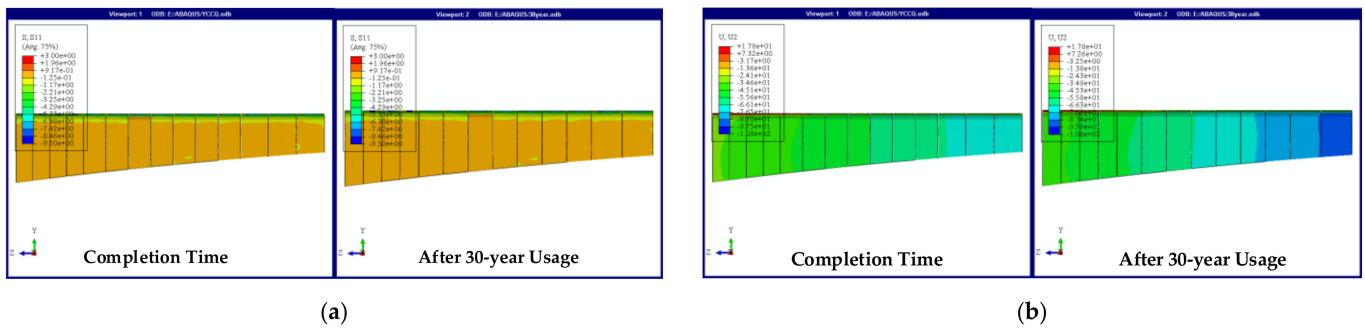


Figure 18. Performance comparison between bridge upon completion and after 30 years' usage. (a) Stress distribution comparison. (b) Displacement distribution comparison.

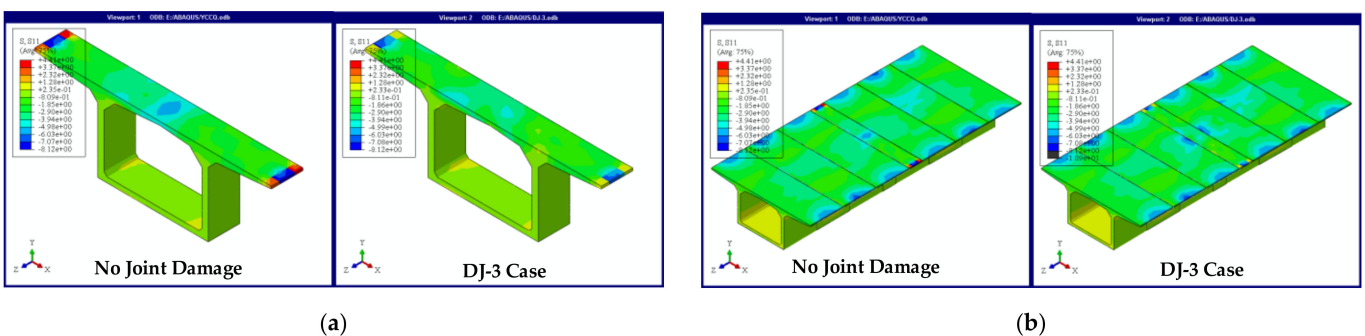


Figure 19. Stress distribution comparison between DJ-3 damage case and no joint damage condition. (a) Single segment. (b) Mid-span range.

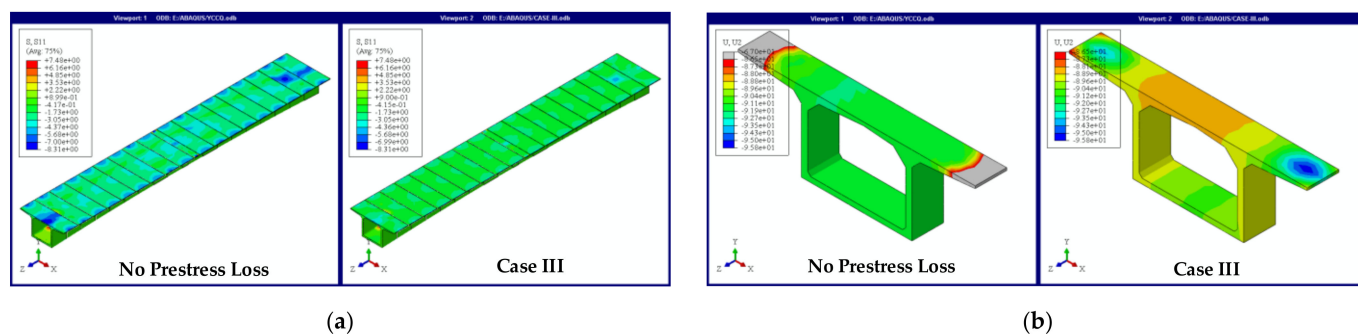


Figure 20. Performance comparison between prestress loss Case III and no-loss condition. (a) Stress distribution from 3/8 to 5/8 span range. (b) Displacement distribution of mid-span segment.

Firstly, the influence of box web crack on local stress was investigated. The stress distribution results of perfect and cracked box girder elements at the same location are presented in Figure 17a. It is evident that the occurrence of a crack within the box girder leads to local stress redistribution, with the region of tension failure (stress exceeding 3 MPa) initially occurring adjacent to and below the position of the crack. Additionally, with the appearance of cracks, the uneven degree of stress distribution increased and stress concentration appeared near the crack location. The impact range of concrete cracking in a single section on the structural stress contour is summarized in Figure 17b. It can be observed that the effect of box girder crack at the quarter point on stress distribution was limited, and there was a more pronounced redistribution of stress on the left side of the crack than on the right side, indicating that web cracks have a greater effect on shear-moment coupling zone mechanical properties.

Figure 18 depicts the axial stress and vertical displacement distribution under different loading ages of concrete. It can be concluded that the amplitude and distribution law were similar under different concrete creep ages, except for the displacement value. It is suggested that the time-dependent behavior of concrete has little impact on the overall distribution of structural stiffness, with only a slight reduction in stiffness observed.

The stress distribution of the superstructure with and without joint damage was also investigated, and the result is presented in Figure 19. Two conclusions can be found: (a) From the perspective of a single segment at the joint damage location in Figure 19a, it can be observed that the stress amplitude on the top plate of the box girder decreased due to adjacent joint damage. This indicates a reduction in load-bearing proportions for the segment, resulting from a loss of connection stiffness. (b) As the load proportion on the mid-span segment decreases, stress will be transferred to its adjacent segments, as illustrated in Figure 19b. Furthermore, joint-degradation-induced stress redistribution had a limited impact on distant segments, at least under current applied vehicle loads.

Actually, the impact of joint damage is generally significant for small-span CPR bridges. The reason for this is that in the case of a small span, the proportion of shear force acting on the beam becomes greater, thereby amplifying the significance of shear stiffness loss caused by joint damage. In this case, the necessary solutions should be implemented when adjacent beam connection failures occur. The failure of concrete joints is typically categorized into three types: longitudinal bridge separation, the vertical displacement of joints and the transverse shifting of joints. To address the issue of longitudinal bridge separation in joints, the most effective approach generally involves applying external prestressed tendons or installing steel plates or CFRP sheets at the joint location. In terms of addressing the vertical displacement and transverse shifting of joints, increasing the friction coefficient between joints can be achieved by incorporating concrete tooth blocks or shear keys at the joint position to prevent any dislocation between them.

The previous argument suggests that the impact of horizontal and vertical prestress loss on the overall stiffness of the structure is limited. However, it has a significant effect on the local stress of segments, as demonstrated in Figure 20a. The reduction in transverse

prestress resulted in a significant decrease in residual compressive stress within the box girder, thereby inducing an increase in local deformation, especially in the cantilever position on both sides of the top plate, which can be clearly verified in Figure 20b. The increase in displacement was positively correlated with the loss rate.

The loss of longitudinal prestress has a significant impact on both global and local stresses. Figure 21a illustrates the distribution law of principal stress flow in the 270 m main span of the bridge, where the blue arrow indicates the direction of larger compressive stress flow. The results indicate that the proportion of maximum stress at the end decreased significantly with longitudinal prestress loss, while only limited changes in the amplitude and direction of stress flow were witnessed at other positions along the main span. As all longitudinal prestressed steel strands of the top and bottom plates traversed through the mid-span section, the loss in longitudinal prestress had the most pronounced impact on the mid-span local stress distribution. The stress, considering the 29% prestress loss in the mid-span section, is illustrated in Figure 21b, indicating a reduction in stress at both the top and bottom plates compared to the no-loss condition.

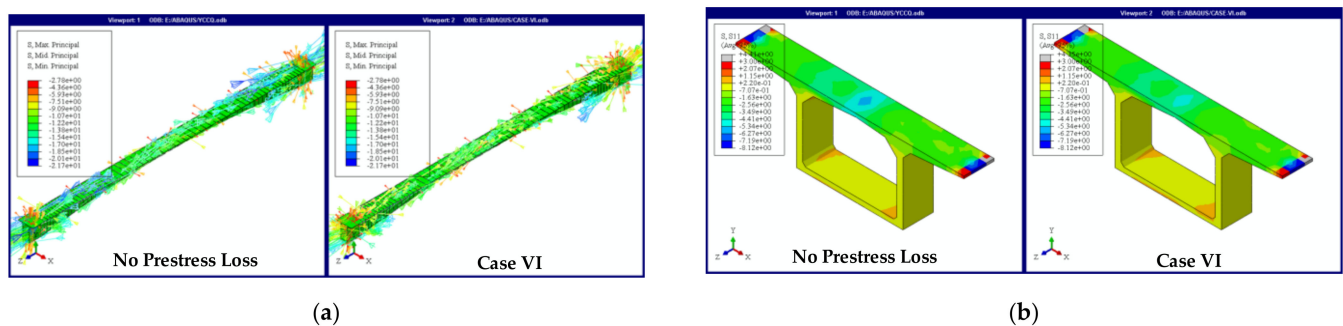


Figure 21. Stress distribution comparison between prestress loss Case VI and no-loss condition. (a) Main span range. (b) Mid-span segment.

By comparing the above factors, it can be concluded that the occurrence of bridge defects will have an impact on the local mechanical properties of the box girder in the large-span CPCRC bridge, among which the transverse and longitudinal prestress combination loss has the biggest influence, and the change in local stress caused by the time-dependent property of concrete has the least.

From the perspective of the influence range of local stress, the stress redistribution caused by box girder cracking was more extensive than that caused by joint damage. Therefore, for bridges with segmental joint damage, the bridge performance can be maintained by only reinforcing the corresponding segmental joint. It is insufficient to only reinforce the location of the crack in the event of structural cracks occurring within the bridge beam, however. It is imperative to also consider the redistribution of stress caused by said cracks, whose influence range is contingent upon factors such as cracking location, load amplitude and section stiffness. Targeted repair measures must be implemented based on their respective stress impact ranges so as to prevent the further propagation of existing fissures.

It should be noted that the objective of our paper was to analyze the relative influence of different factors on the long-term deflection of the structure under its completed state, rather than determining its real stress during construction. In other words, the model established in this paper is limited to analyzing the relative change law of stress and displacement. However, it lacks practical significance in terms of determining the absolute value of local stress due to its failure to consider factors such as initial internal force accumulation caused by the construction process, material nonlinearity, and the redistribution of bending stress due to creep. Therefore, if an accurate investigation of the real stress distribution of the box girder is required, these aforementioned factors must be taken into consideration within the refined model.

5. Conclusions

In this study, the causes of long-term deflection in large-span continuous prestressed concrete rigid-frame (CPCR) bridges were analyzed through field monitoring and refined modeling techniques. The main conclusions are summarized as follows:

1. An accurate refined modelling approach that takes into account reinforcement behavior and various performance degradation behaviors has been elaborated to simulate the behavior of large-span CPCR bridges. The proposed finite element model has been validated by comparing predicted results with field monitoring data from a 270 m CPCR bridge in China over the past two decades, with a maximum error smaller than 5%.
2. A sensitivity analysis of different damage conditions on the CPCR bridge performance was carried out. It can be concluded that the primary cause for long-lasting deflection in large-span CPCR frame bridges is attributable to the time-dependent loss of longitudinal prestress. For the validated model proposed in this paper, the maximum vertical deflection increased by 190% when the longitudinal prestress loss reached approximately 30% in this model.
3. The sensitivities to the impact on the overall performance of the structure ranged from significant to slight: longitudinal prestress loss, box girder crack, concrete creep, continuous joint damage, horizontal and vertical prestress loss, and discrete joint damage, respectively.
4. The impact of joint damage was highly related to the span length of the bridge. In the case of a small span, the proportion of shear force acting on the beam becomes greater, thereby amplifying the significance of shear stiffness loss caused by joint damage. For long-span CPCR bridges, however, the section bending moment dominates and limits the effects of joint damage on structural integrity.
5. Local displacement and stress distribution are significantly influenced by typical structural damage, and the affected areas are different. For CPCR bridges with segmental joint damage, reinforcing the corresponding joint is sufficient to maintain bridge performance. Reinforcing the crack location alone is insufficient when structural cracks appear in the beam. Remediation measures must be tailored to the respective stress redistribution zones to prevent the further expansion of existing cracks.

Author Contributions: Conceptualization, X.H. and W.L.; methodology, X.H.; software/simulation, X.H. and P.L.; validation, X.H., W.L. and P.L.; formal analysis, X.H.; investigation, W.L. and P.L.; writing—original draft preparation, X.H.; writing—review and editing, W.L.; supervision, W.L.; project administration, P.L. All authors have read and agreed to the published version of the manuscript.

Funding: This research was funded by the Research Institute of the Highway Ministry of Transport and the “Key Technology Research of Guanfo Expressway Maintenance Engineering” project (0222KF06SC1123).

Institutional Review Board Statement: Not applicable.

Informed Consent Statement: Not applicable.

Data Availability Statement: Data from this study can be made available upon request.

Acknowledgments: This work was funded by the “Key Technology Research of Guanfo Expressway Maintenance Engineering” project. In addition, we thank Xinmin Zhang (X.Z.), who works in the Guangzhou-Shenzhen Expressway Reconstruction and Expansion Management Office, for help provided during the research.

Conflicts of Interest: The authors declare no conflict of interest.

References

1. Yang, Y.X. Analysis of Stress Measuring and Testing of Continuous Rigid Frame Bridge. *Adv. Mater. Res.* **2012**, *346*, 787–792. [[CrossRef](#)]
2. Wang, H.C.X.; Liu, D.; Qin, S. Continuous Reinforced Concrete Rigid-Frame Bridges in China. *Pract. Period. Struct. Des. Constr.* **2019**, *24*, 05019002. [[CrossRef](#)]
3. Liu, Y.S.H.; Ye, L.; Lu, X.; Zhang, X. Experiment and damage evaluation on a large-scale continuous rigid frame bridge model. *Eng. Mech.* **2007**, *35*, 124–130. (In Chinese)
4. Zong, Z.X.; Liu, H.; Li, Y.; Huang, X. Collapse Failure of Prestressed Concrete Continuous Rigid-Frame Bridge under Strong Earthquake Excitation: Testing and Simulation. *J. Bridge Eng.* **2016**, *21*, 04016047. [[CrossRef](#)]
5. Tong, L.; Wang, R.; Wang, D. Seismic cracking mechanism and control for pre-stressed concrete box girders of continuous rigid-frame bridges: Miaoziping bridge in Wenchuan earthquake as an example. *Adv. Bridge Eng.* **2021**, *2*, 17. [[CrossRef](#)]
6. Zheng, H.B.; Yu, X.L.; Hu, J.L.; Yan, Q.S. Parameter Sensitivity Analysis of Vertical Deflection for Long-Span Continuous Rigid-Frame Bridge. *Adv. Mater. Res.* **2011**, *163*, 1500–1504. [[CrossRef](#)]
7. Guo, F.; Yang, Y.Q.; Huang, S.Q. Research on Deflection and Cracking of Prestressed Concrete Continuous Girder Bridge. *Adv. Mater. Res.* **2013**, *838*, 1014–1017. [[CrossRef](#)]
8. Ruiz, M.F.; Muttoni, A.; Gambarova, P.G. Relationship between Nonlinear Creep and Cracking of Concrete under Uniaxial Compression. *J. Adv. Concr. Technol.* **2007**, *5*, 383–393. [[CrossRef](#)]
9. Zhao, T.; Lei, J.Q. Research on the shrinkage and creep of the long-span continuous rigid frame bridge for the high-speed railway. In Proceedings of the 1st International Conference on Railway Engineering: High-speed Railway, Heavy Haul Railway and Urban Rail Transit, Beijing, China, 20–21 August 2010; pp. 858–863.
10. He, G.J.; Li, Y.Y.; Zou, Z.Q.; Duan, L.L. Effect of concrete creep on pre-camber of continuous rigid-frame bridge. *J. Cent. South Univ. Technol.* **2008**, *15*, 337–341. [[CrossRef](#)]
11. Yan, B.; Zhang, G.; Xie, H. Interaction Between Tracks and Continuous Rigid-frame Bridge Carrying Railway Under Action of Shrinkage and Creep. *J. China Railw. Soc.* **2017**, *39*, 99–103.
12. Scordelis, A.C. Computer Models for Nonlinear Analysis of Reinforced and Prestressed Concrete Structures. *Pci J.* **1984**, *29*, 116–135. [[CrossRef](#)]
13. Han, X.; Fernando, D.; Han, B. Numerical modelling of the in-plane behaviour of concrete-filled circular steel tubular arches. *Constr. Build. Mater.* **2020**, *264*, 1–19. [[CrossRef](#)]
14. Huang, S.N.; Lu, X.Z.; Ye, L.P.; Liu, Y.K. Nonlinear finite element analysis for a prestressed continuous rigid frame concrete bridge. In Proceedings of the International Symposium Computational Mechanics, Hong Kong, China, 30 November–3 December 2009; Springer: Beijing, China, 2009; p. 267. [[CrossRef](#)]
15. Yuan, Z.; Ng, P.L.; Bačinskis, D.; Du, J. Analysis of Non-Uniform Shrinkage Effect in Box Girder Sections for Long-Span Continuous Rigid Frame Bridge. *Balt. J. Road Bridge Eng.* **2018**, *13*, 146–155. [[CrossRef](#)]
16. Li, S.; Yang, Y.; Pu, Q.; Yang, D.; Sun, B.; Li, X. Three-dimensional nonlinear creep and shrinkage effects of a long-span prestressed concrete box girder bridge. *Struct. Concr.* **2019**, *20*, 638–649. [[CrossRef](#)]
17. Zhang, N.H.; Xing, J.J. An alternative model for elastic bending deformation of multilayered beams. *J. Appl. Phys.* **2006**, *100*, 103519. [[CrossRef](#)]
18. Lin, L.X.; Zhang, Y.H.; Wu, Y.P.; Ding, N.H. Approximate deflection calculation of variable box section girder considering the effect of shear lag and shear deformation. In Proceedings of the International Conference on Civil Engineering and Building Materials (CEBM), Kunming, China, 29–31 July 2011; pp. 967–971.
19. El-Badry, M.; Ghali, A. Serviceability Design of Continuous Prestressed Concrete Structures. *Pci J.* **1989**, *34*, 54–91.
20. Yu, J.; Zhang, J.; Li, P.; Han, X. Influence of Superstructure Pouring Concrete Volume Deviation on Bridge Performance: A Case Study. *Buildings* **2023**, *13*, 887. [[CrossRef](#)]
21. Liu, S.; Zhang, Y.; Shi, J.; Yang, B. Internal Forces Analysis of Prestressed Concrete Box Girder Bridge by Using Structural Stressing State Theory. *Materials* **2021**, *14*, 4671. [[CrossRef](#)]
22. Han, X.; Xie, H.; Yan, W.; Ma, Q. Experimental and numerical study on the in-plane behaviour of concrete-filled steel tubular arches with long-term effects. *Thin-Walled Struct.* **2021**, *169*, 108507. [[CrossRef](#)]
23. Long, Y.; Zhang, C.; Zhou, Y. A Comparative Study for Concrete Fracture Analysis Using Smeared- and Discrete-Crack Model. *Eng. Mech.* **2008**, *25*, 80–84. (In Chinese)
24. Lam, T.-Q.-K.; Do, T.-M.-D.; Ngo, V.T.; Nguyen, T.T.N.; Pham, D.Q. Concrete grade change in the layers of three-layer steel fibre reinforced concrete beams. *J. Achiev. Mater. Manuf. Eng.* **2020**, *1*, 16–29. [[CrossRef](#)]
25. Trost, H. Effects of the superposition principle on creep and relaxation problems in concrete and prestressed concrete. *Concr. Reinf. Concr. Constr.* **1967**, *10*, 230–238. (In German)
26. Zdenek, P.B. Prediction of Concrete Creep Effects Using Age-Adjusted Effective Modulus Method. *ACI J. Proc.* **1972**, *69*, 212–217. [[CrossRef](#)]
27. Ministry of Transport of China. *General Specification for Design of Highway Bridges and Culverts*; China Communications Press: Beijing, China, 2015.
28. Birkeland, P.W.; Birkeland, H.W. Connections in Precast Concrete Construction. *ACI J. Proc.* **1966**, *63*, 345–368. [[CrossRef](#)]
29. Hofbeck, J.A.; Alan, I.O.I. Shear Transfer in Reinforced Concrete. *ACI J. Proc.* **1969**, *66*, 119–128. [[CrossRef](#)]

30. Magura, D.D.; Sozen, M.; Siess, C.P. A Study of Stress Relaxation in Prestressing Reinforcement. *Pci J.* **1964**, *9*, 13–57. [[CrossRef](#)]
31. Zheng, Y.; Kosa, K.; Fukunaga, Y.; Kusano, M. Estimation of Effective Prestress based on Stress-releasing Method and FEM Analysis of the Method. *J. Struct. Eng.* **2012**, *58*, 599–610. [[CrossRef](#)]
32. Moravčík, M.; Kralovanec, J. Determination of Prestress Losses in Existing Pre-Tensioned Structures Using Bayesian Approach. *Materials* **2022**, *15*, 3548. [[CrossRef](#)]
33. Zhou, Y.Z.; Zhao, Y.; Li, Z.J. Computing method for effective pre-stress testerbased on transverse tensioning method. *J. Hefei Univ. Technol.* **2013**, *36*, 248–252. (In Chinese) [[CrossRef](#)]
34. Noyan, I.C.; Cohen, J.B. *Residual Stress. Measurement by Diffraction and Interpretation*; Springer: Berlin/Heidelberg, Germany, 1987.
35. Tanaka, K.; Suzuki, K.; Akiniwa, Y. *Evaluation of Residual Stresses by X-ray Diffraction*; Yokendo: Bunkyo, Tokyo, 2006. (In Japanese)
36. Tanaka, K. The $\cos\alpha$ method for X-ray residual stress measurement using two-dimensional detector. *Mech. Eng. Rev.* **2019**, *6*, 18-00378. [[CrossRef](#)]
37. Wang, G.L.; Fu, Y.F. Investigation on Crack of Long-span Prestressed Concrete Box Girder Bridges in Service. *J. Highw. Transp. Res. Dev. (Engl. Ed.)* **2009**, *4*, 71–76. [[CrossRef](#)]

Disclaimer/Publisher’s Note: The statements, opinions and data contained in all publications are solely those of the individual author(s) and contributor(s) and not of MDPI and/or the editor(s). MDPI and/or the editor(s) disclaim responsibility for any injury to people or property resulting from any ideas, methods, instructions or products referred to in the content.